




A facile impregnation synthesis of Ni-doped TiO₂ nanomaterials for dye-sensitized solar cells

Tharmakularasa Rajaramanan^{1,2}, Dhayalan Velauthapillai^{1,*} , Punniamoorthy Ravirajan², and Meena Senthilnanthanan^{3,*}

¹ Faculty of Engineering and Science, Western Norway University of Applied Sciences, P.O. Box 7030, 5020 Bergen, Norway

² Clean Energy Research Laboratory, Department of Physics, University of Jaffna, Jaffna 40000, Sri Lanka

³ Department of Chemistry, University of Jaffna, Jaffna 40000, Sri Lanka

Received: 28 January 2023

Accepted: 25 March 2023

Published online:

8 April 2023

© The Author(s) 2023

ABSTRACT

This study reports a facile impregnation method for synthesizing Ni-doped TiO₂ nanomaterials using P25-TiO₂ as a starting material. The as prepared nanomaterials were subjected to structural and optical characterizations and subsequently employed in photovoltaic studies. X-ray diffraction (XRD) and Raman studies confirmed that Ni doping did not alter the anatase and rutile contents of P25-TiO₂. Also, the presence of the constituent dopants and their ionic states were confirmed by Energy-Dispersive X-ray (EDX) and X-ray photoelectron (XPS) spectroscopies. Topographic Atomic Force Microscopic (AFM) images illustrated that Ni doping had increased the surface roughness of the TiO₂. Optical characterization by UV-Visible spectroscopy revealed that the Ni doping had caused red shift in light absorption due to reduced TiO₂ bandgap and improved the dye adsorption on TiO₂ films. Then, the photocurrent–photovoltage property of the fabricated devices was investigated and the optimized 0.10 wt% Ni-doped TiO₂ photoanode based device exhibited pronounced power conversion efficiency (PCE) of 6.29% under air mass (AM) 1.5 conditions (100 mWcm⁻², 1 sun). Improved charge transport properties were also observed by the electrochemical impedance spectroscopic (EIS) study for the device with optimized Ni-doped TiO₂ compared to the control device.

1 Introduction

Dye-sensitized solar cells (DSSCs) have become a significant topic in the field of solar photovoltaic technology for three decades because of their cost-effectiveness, eco-friendliness and working ability under low intensity light conditions [1]. It consists of

an electrode with a mesoporous wide bandgap semiconductor sensitized with a light absorbing dye, a redox electrolyte and a counter electrode made up of platinized conductive glass [2]. TiO₂ is widely used as the semiconductor in DSSC due to its' porous nature, non-toxic and uncomplicated preparation methods and ability to easily combine with other

Address correspondence to E-mail: Dhayalan.Velauthapillai@hvl.no; meena@univ.jfn.ac.lk

metal oxides or dopants [3]. However, its overall performance in the photovoltaic application is still limited due to poor electron mobility of nano porous TiO₂ [4] and limited solar spectral response of the dye in the visible region [5, 6]. In the literature, various attempts have been reported to overcome these limitations by placing a compact metal oxide blocking layer on the Transparent Conducting Oxide (TCO), coating the TiO₂ film with a thin layer of a wide band gap semiconductor, forming composites with TiO₂ electrode, modifying the morphology of nanostructured semiconductors using self-assembled monolayer [7] / insulator [8] and doping/co-doping the TiO₂ with other elements [9].

Many studies have reported the promising effect of dopants on the TiO₂ based DSSCs. Among the effective dopants, transition metals (Zn [5, 10], Ag [11], Nb [12], W [13], Cu [14], etc.) are found to be superior to non-transition elements as they improve light absorption and electrical conductivity by incorporating new impurity energy levels within the TiO₂ band gap or modifying the conduction band or valence band of the TiO₂ [15, 16]. Among the transition elements, it is noted that high electrical conductivity of Nickel (Ni) prevents loss of electrons during electron transfer and thus increases the current density and efficiency of DSSCs when used as a dopant [17]. Also, Ni doping on TiO₂ improves visible light harvest through a red shift in the wavelength of absorption of the solar radiation [18].

Many studies on the influence of Ni-doped TiO₂ on the performance of DSSCs are reported in the literature. Power conversion efficiencies (PCEs) of 2.86%, 3.60% and 4.04% were demonstrated for DSSCs fabricated with Ni-doped TiO₂ photoanode, where the doped nanomaterial was synthesized by sol-gel method [19–21]. In a separate study, Malik and his group has reported that hydrothermally synthesized Ni-doped TiO₂ based device increases the photovoltaic current and hence improves the device efficiency up to 6.72% [22]. A common feature in all the above doping methods is the treatment of Ni dopant with a titanium precursor. Alternatively, doping could be achieved by treating the Ni dopant with pre-made TiO₂. Moreover, the method of doping also plays a crucial role in altering the properties of the TiO₂ which in turn strongly influences the corresponding DSSC performance.

So far, the treatment of Ni dopant with the pre-made TiO₂ (P25-TiO₂) nanomaterial and its influence

on the device performance have not been investigated. Hence, an attempt was made to synthesize the Ni-doped TiO₂ nanomaterial by a facile wet impregnation method using commercially available P25-TiO₂ and NiCl₂·6H₂O. This is a very simple approach which involves introduction of the dopant atoms directly into the pre-made TiO₂ lattice in a liquid solvent and subsequent removal of the solvent at high temperature.

2 Materials and methods

2.1 Synthesis of Ni-doped TiO₂ nanomaterials

Initially, 1 g of P25-TiO₂ nanopowder (21 nm primary particle size, $\geq 99.5\%$ trace metals basis, Sigma-Aldrich) was dispersed into ethanol ($> 99\%$, Sigma Aldrich) and the resulting TiO₂ slurry was stirred for 1 h. Then, 0.05, 0.10, 0.50 and 1.00 wt% of Ni²⁺ solutions were prepared by dissolving the respective amounts of NiCl₂·6H₂O (99.9%, Sigma-Aldrich) in ethanol separately. Subsequently, the prepared Ni²⁺ solutions were individually mixed with the TiO₂ slurry and stirred vigorously for 2 h to obtain the respective Ni-TiO₂ mixtures, which were dried at 100 °C and ground well using Agate mortar and pestle to obtain a fine powder. The above products were calcinated at 500 °C for 2 h and Ni-doped TiO₂ nanomaterials were synthesized (Fig. 1). Finally, the DSSC was fabricated as reported in our previous study [23].

2.2 Characterization of the synthesized nanomaterials

The crystalline structures of all the Ni-doped and undoped TiO₂ nanomaterials were explored by X-ray diffraction spectroscopy (XRD, PANalytical-AERIS, Almelo, Netherlands). The diffraction pattern was collected with Cu K α radiation ($\lambda = 1.5408 \text{ \AA}$) at ambient temperature, under the accelerated voltage of 40 kV; emission current of 44 mA; scan range (2θ) between 10° and 90° with a step size of 0.0027° and a scan speed of 4°/min. Raman spectroscopic measurements were analyzed using a laser confocal Raman microscope (Renishaw, UK, Model: Invia). The elemental analysis of the nanomaterials was studied by Energy Dispersive analysis of X-ray

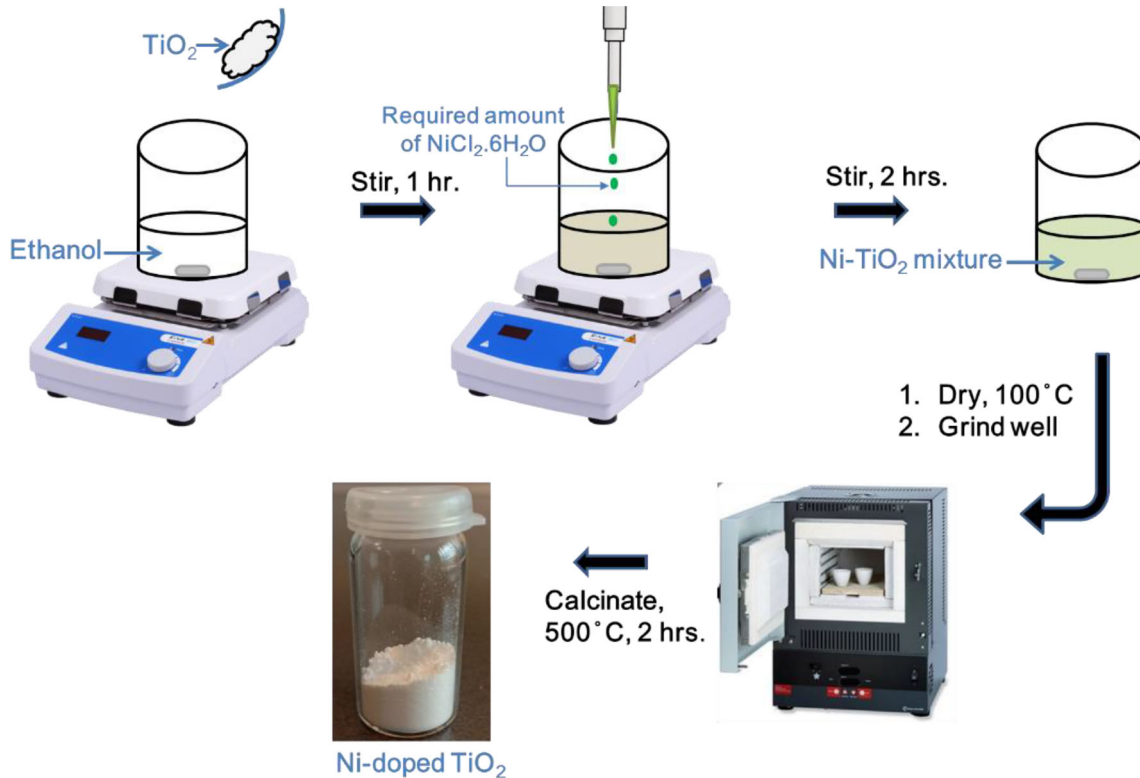


Fig. 1 Schematic diagram of synthesis of Ni-doped TiO_2 nanomaterial

technique (Bruker EDX analyser). The surface electronic state of the Ni-doped TiO_2 was determined by X-ray photoelectron spectroscopy (XPS, Kratos Axis Ultra DLD). The surface nature of the nanomaterials was investigated using atomic force microscopy (Park XE7, Korea). Absorption spectra of all the synthesized nanomaterials were recorded using a JENWAY 6800 UV-Visible Spectrophotometer (OSA, UK) controlled by Flight Deck software. The photovoltaic performance of all the fabricated devices with an effective area of 0.25 cm^2 was studied using Keithley-2400 source meter under simulated irradiation of 1 sun illumination intensity (100 mW/cm^2) by 150 W Xe lamp with AM 1.5 filter (Pecell-PEC-L12, Kanagawa, Japan). The charge transport properties of the devices were measured by electrochemical impedance spectroscopy (EIS) at the frequency range from 10^{-2} to 10^6 Hz under light condition using a Metrohm Autolab Potentiostat/galvanostat (PGSTAT 128 N, Utrecht, Netherlands) with a FRA 32 M Frequency Response Analyzer (FRA).

3 Results and discussion

3.1 Structural properties of Ni-doped TiO_2 nanomaterial

Figure 2a reveals the X-ray diffraction results of the un-doped TiO_2 and 0.05, 0.10, 0.50 and 1.00 wt% Ni-doped TiO_2 films. The XRD patterns of all the fabricated films exhibited peaks at 25.20° , 37.60° , 48.20° , 53.70° , 55.00° , 62.50° , 68.50° , 70.20° , 74.89° and 82.53° corresponding to the reflection planes of (101), (004), (200), (105), (211), (204), (116), (220), (215) and (224) for anatase TiO_2 phase, while peaks at 27.39° , 36.07° and 41.2° correspond to the reflection planes of (110), (101) and (111) for rutile TiO_2 phase. The obtained values match well with the anatase XRD JCPDS Card No. 21-1272 and rutile JCPDS Card No. 21-1276 respectively [24].

All Ni-doped and un-doped TiO_2 show the same anatase and rutile peaks, confirming that phase transition in TiO_2 had not taken place during Ni doping. This could be attributed to the similarity in the ionic radii of Ni^{2+} (0.072 nm) and Ti^{4+} (0.068 nm) [25] that leads to replacement of Ti^{4+} ions in the lattice by Ni^{2+} ions. The average crystallite size of the

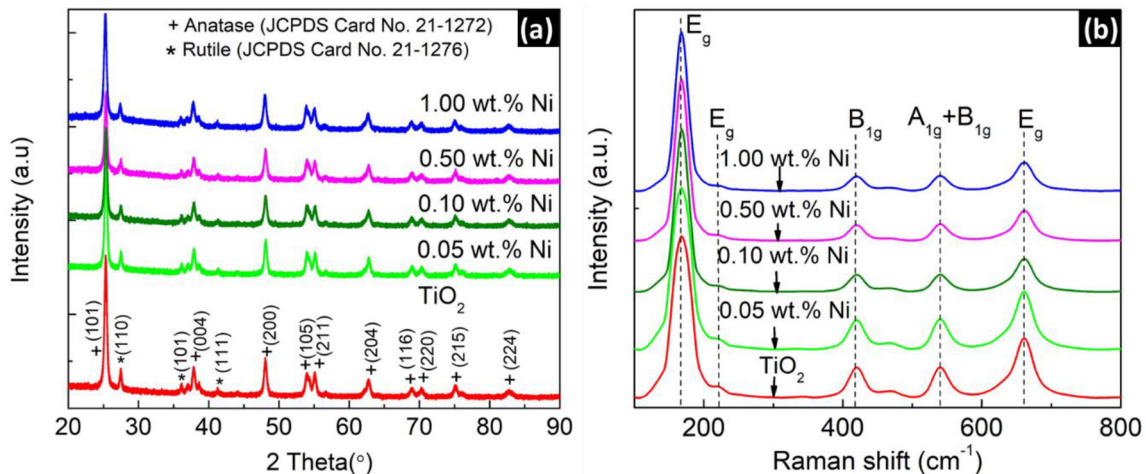


Fig. 2 **a** XRD patterns of the un-doped, 0.05, 0.10, 0.50 and 1.00 wt% Ni-doped TiO₂ films, and **b** Raman spectra of the same films

synthesized nanomaterials was calculated by the Scherrer equation using anatase (101) plane as reported in our previous study [23]. The approximate crystallite sizes (*d*) of un-doped, 0.05, 0.10, 0.50 and 1.00 wt% Ni-doped TiO₂ nanomaterials were found to be 18.3, 18.2, 17.6, 17.5 and 16.5 nm respectively. The reduction in crystallite size would have resulted due to the shorter Ni–O bond distance (1.87 Å) than that of Ti–O bond (1.94 Å) [26]. Similar inhibitory trends have been reported by Alijani and her co-worker with respect to the growth of crystallite size and anatase-rutile phase transformation due to Ni doping [27]. The absence of crystallite peaks of Ni in the XRD of the synthesized Ni-doped TiO₂ may be due to the low concentrations of Ni dopant. Raman spectroscopy was carried out in the range from 100 to 800 cm⁻¹ to further confirm the crystallinity of the synthesized nanomaterials and the results are shown in Fig. 2b. Generally, the Raman spectrum of TiO₂ nanomaterial shows five bands corresponding to the six Raman active modes of TiO₂. Well resolved Raman peaks with the D_{4h} space group at about 170, 216, and 657 cm⁻¹ (E_g), 539 cm⁻¹ (A_{1g} + B_{1g}), and 420 cm⁻¹ (B_{1g}) corresponding to the anatase phase of TiO₂ were observed [23]. The absence of peaks for Ni and crystalline oxides of Ni could be attributed to the low concentration of Ni which is in consistent with the XRD results. A reduction in the intensity of the peaks of Raman spectra was observed with increasing amounts of Ni dopant which indicates the impact of interaction between TiO₂ and Ni on the Raman resonance of TiO₂. Similar effect of Ni doping on the intensity of TiO₂ peaks is reported in the literature

[21]. To confirm the existence of Ni dopant in the Ni-doped TiO₂ nanomaterials, EDX and XPS spectroscopies were carried out.

Figure 3a–e exhibit EDX spectra of the un-doped and all Ni-doped TiO₂ nanomaterials in the binding energy range from 0.0 to 20.0 KeV. The results reveal the presence of Ti, O and Ni in the Ni-doped TiO₂ nanomaterials and the amount of Ni increases with the increasing amount of Ni dopant (Table 1). Further, EDX mapping of the optimized Ni-doped TiO₂ (0.10 wt%) illustrates extensive dispersion of Ti, O and Ni elements confirming that Ni is well-distributed on the surface of TiO₂ (Fig. 3f). Further, XPS study was performed to confirm the electronic state of the dopant in the Ni-doped TiO₂ nanomaterials.

Figure 4 represents XPS spectrum of the optimized 0.10 wt% of Ni-TiO₂ nanomaterial consisting of Ti, O, and Ni elements. As reported in our previous study, the 2p_{3/2} and 2p_{1/2} peaks in the Ti 2p spectrum are characteristic of titanium dioxide. The peaks located at 455.7 and 461.4 eV belong to Ti 2p spin-orbit splitting photoelectrons of Ti⁴⁺ ions. Also, the binding energy at 526.9 eV of O 1s photoelectron confirms the presence of O²⁻ state in the nanoparticles [28]. The peak for the Ni 2p_{3/2} located at 852.73 eV is characteristic of metallic Ni which could be mainly attributed to the alloy substrate [29]. Moreover, it is reported in the literature that peaks at 858.4 and 870.5 eV represent the Ni 2p_{3/2} and Ni 2p_{1/2} photoelectrons respectively which are responsible for the Ni²⁺ or Ni–O species [30, 31]. Hence, doping of Ni in the TiO₂ lattice is confirmed as per the XPS study. Further, it is noteworthy to mention that the

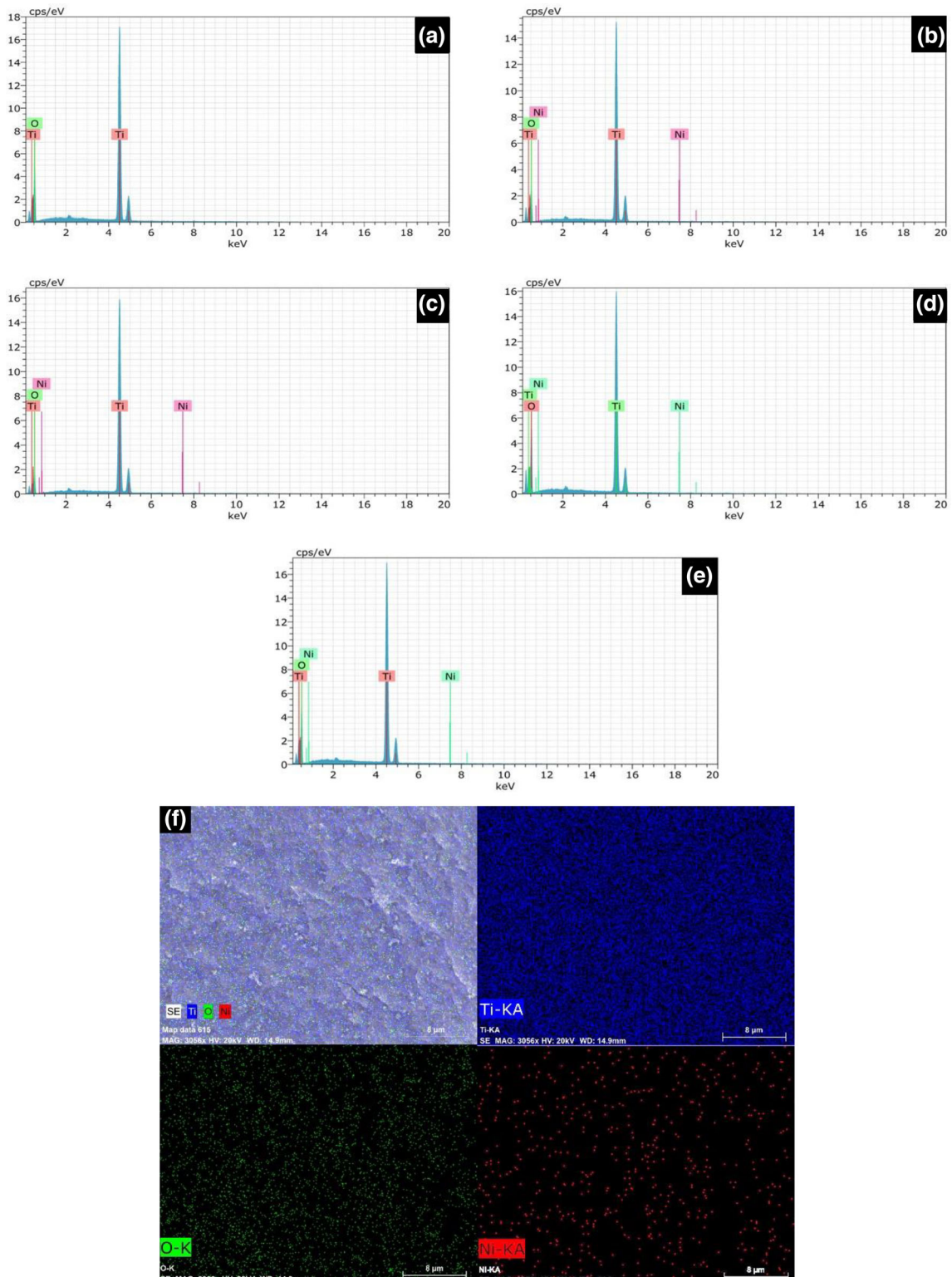


Fig. 3 a–e EDX spectra of un-doped, 0.05, 0.10, 0.50 and 1.00 wt% Ni-doped TiO₂ nanomaterials, and f EDX-mapping of 0.10 wt% Ni-doped TiO₂ nanomaterial

Table 1 Weight percentages of Ni in the un-doped and Ni-doped TiO₂ nanomaterials according to the EDX investigation

Sample	wt% of Ni (EDX results)
Un-doped TiO ₂	0.00
0.05 wt% Ni	0.03
0.10 wt% Ni	0.12
0.50 wt% Ni	0.42
1.00 wt% Ni	0.78

crystallite size reduction observed in the XRD study of Ni-doped TiO₂ due to Ni–O bond formation is also confirmed by the above XPS results.

Then, the effect of the presence of Ni on the nature of TiO₂ surface was examined by atomic force microscopy. Figure 5 shows the 3D and 2D AFM images of the un-doped, 0.05, 0.10, 0.50 and 1.00 wt% of Ni-doped TiO₂ nanomaterials coated films.

According to the AFM images, particles are of spherical shape in all samples and the doping did not change the morphology of TiO₂. Also, the AFM images confirm that Ni doping reduces crystallite size of the TiO₂ and the particle size which further decreases with the increase in dopant concentration, the reason for such observations has already been explained. This is supportive evidence to the XRD results. As a result of the reduction in crystallite size and particle size, the surface roughness (Root mean square) of the film gradually increases from 0.40 μm (for un-doped TiO₂) to 0.76 μm (for 1.00 wt% Ni-doped TiO₂) (Table 2). Higher surface roughness helps to adsorb more dye molecules due to the increased contact area between TiO₂ and the dye molecules layer which in turn facilitates charge transportation in the device. However, it was found that Ni doping beyond 0.10 wt% negatively affects the dye adsorption due to agglomeration of the nanoparticles. In a separate study, Ganesh and his co-researchers has also reported that particles are started

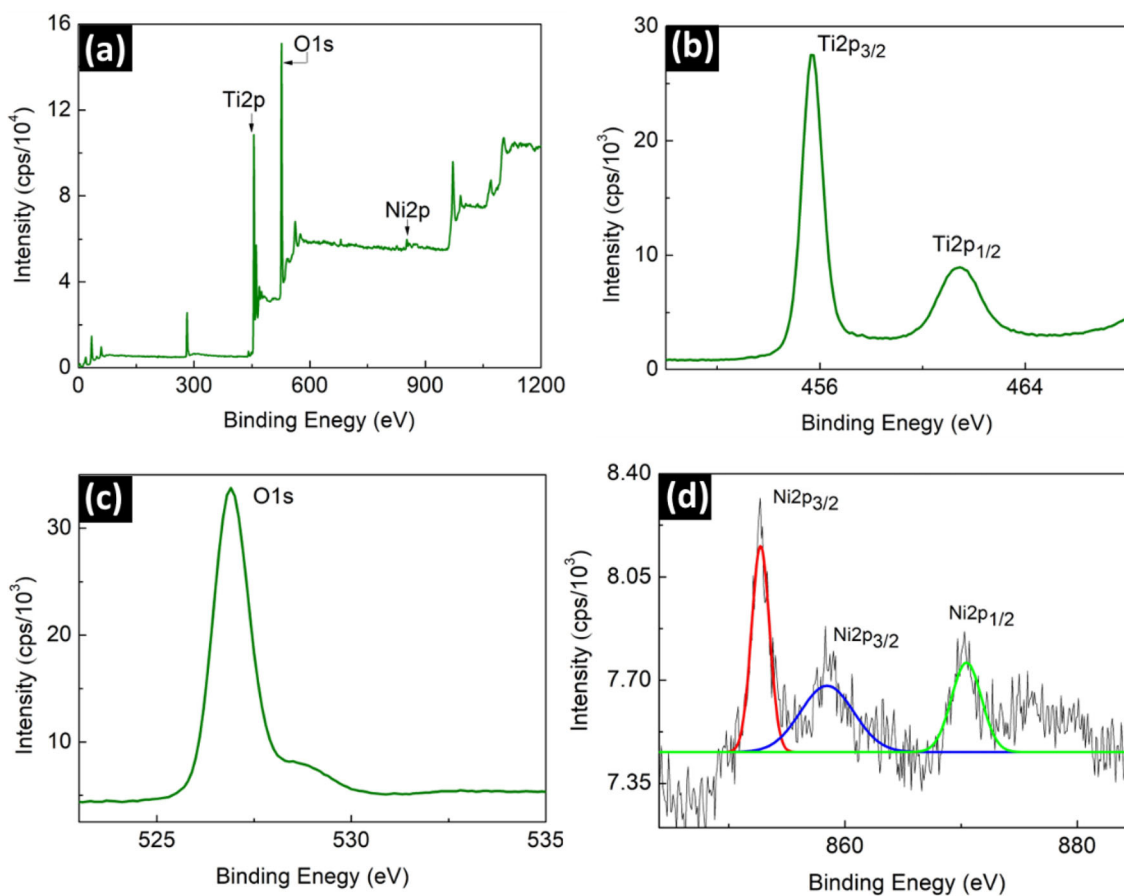
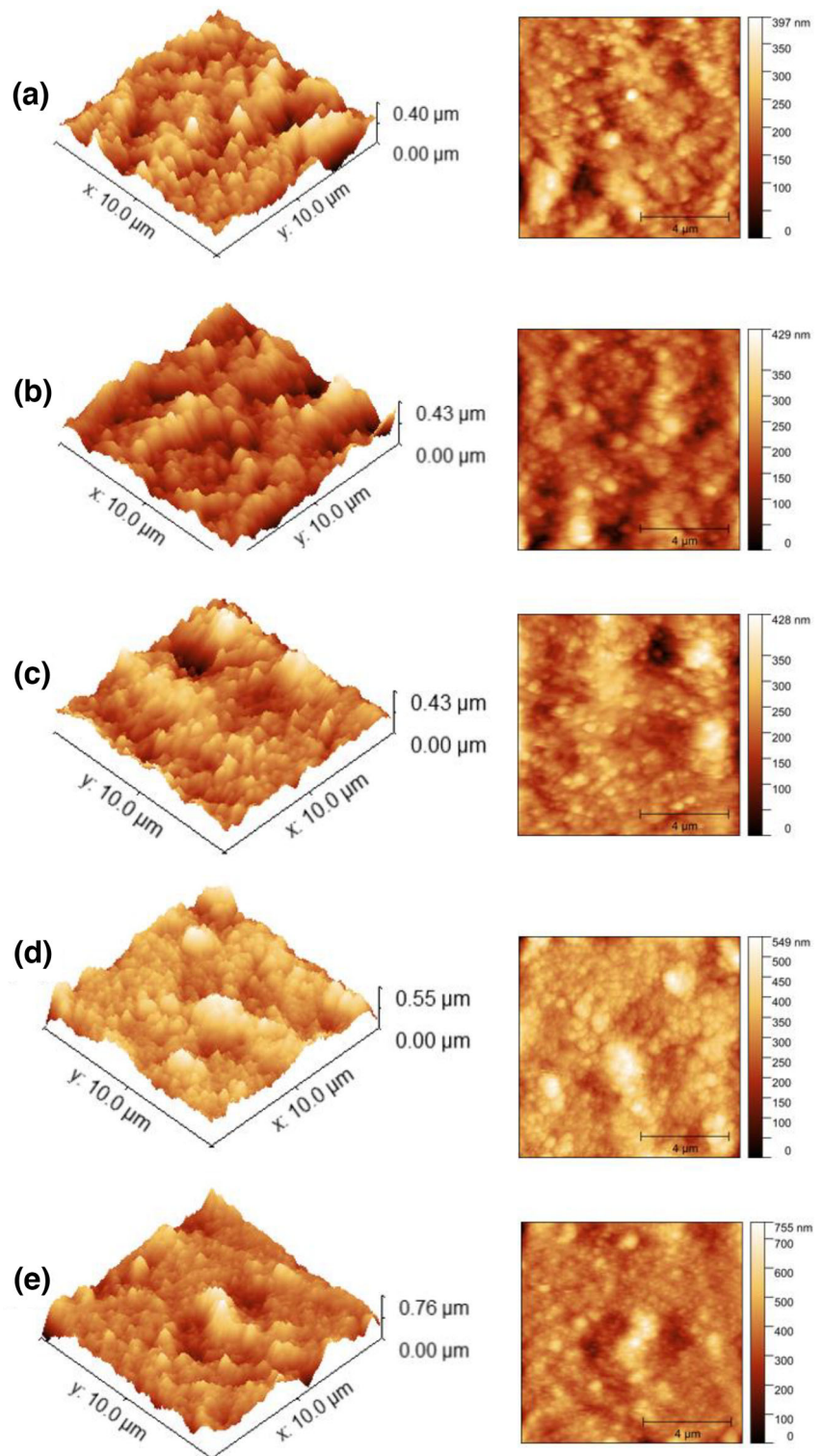
**Fig. 4** a XPS spectrum of 0.10 wt% Ni-doped TiO₂ and b–d high-resolution XPS spectra of Ti 2p, O 1s, and Ni 2p photoelectrons

Fig. 5 a–e 3D and 2D AFM images of a un-doped, b 0.05, c 0.10, d 0.50 and e 1.00 wt% Ni-doped TiO₂ coated films



to agglomerate in higher Ni content in Ni-doped TiO₂ (beyond 0.5 wt%) [32].

3.2 Optical properties of Ni-doped TiO₂ nanomaterial

UV-Visible spectroscopic study was performed to measure the light absorption capacities of un-doped

Table 2 Variation in the crystallite size (d) and root mean square (RMS) roughness of un-doped and all Ni-doped TiO₂ films

Sample	Crystallite size (d, nm)	Root mean square (RMS, μm)
Un-doped TiO ₂	18.3	0.40
0.05 wt% Ni-TiO ₂	18.2	0.43
0.10 wt% Ni-TiO ₂	17.6	0.43
0.50 wt% Ni-TiO ₂	17.5	0.55
1.00 wt% Ni-TiO ₂	16.5	0.76

TiO₂ and 0.05, 0.10, 0.50 and 1.00 wt% Ni-doped TiO₂ and estimate their bandgaps (Fig. 6a, b). Ni-doped TiO₂ showed a gradual shift to longer wavelengths (red shift) in the UV–Visible absorption spectrum with increase in the dopant concentration compared to the un-doped TiO₂ (Fig. 6a). Further, the approximate bandgap values of the above nanomaterials were determined using Tauc plot as reported elsewhere [33, 34], and found to be 3.14, 3.12, 3.08, 2.98 and 2.93 eV for un-doped TiO₂, and 0.05, 0.10, 0.50 and 1.00 wt% for Ni-doped TiO₂ nanomaterials respectively (Fig. 6b).

The observed bandgap narrowing on Ni doping would have predominantly resulted due to creation of an energy level by 3d orbital of Ni just above the valence band thereby uplifting the valence band of TiO₂ which had led to the red shift in the UV-Visible spectrum. It is noteworthy to mention that the influence of Ni (3d) orbital on the conduction band of TiO₂ is lower compared to its valence band [35–37].

The influence of Ni doping on dye adsorption was analyzed by dipping the un-doped and 0.05, 0.10, 0.50 and 1.00 wt% Ni-doped TiO₂ films in the N719 dye for about 12 h and measuring the light

absorption ability of the resultant dye coated films by UV-Visible spectroscopy. The Fig. 7 reveals improved light absorption for dye coated Ni-doped TiO₂ films and the maximum light absorption was attained on 0.10 wt% Ni doping. The better light absorption of dye coated Ni-doped TiO₂ films is ascribed to the increased surface area for dye adsorption because of Ni doping. This was confirmed by increase in surface roughness and slight reduction in particle size due to Ni doping as observed in the respective AFM images. However, further increase in the dopant concentration beyond 0.10 wt% Ni reduced light absorption due to agglomeration of the particles which led to reduction in dye adsorption. These dye adsorption capabilities by Ni-doping also affect the PV properties of the DSSCs, probably the J_{SC} value.

3.3 Photovoltaic performance

The photovoltaic performance of the un-doped and all Ni-doped TiO₂ photoanodes based DSSCs were analyzed by J–V measurements under air mass (AM) 1.5 conditions (100 mWcm⁻², 1 sun) and the results are summarized in Fig. 8a and Table 3. The J–V

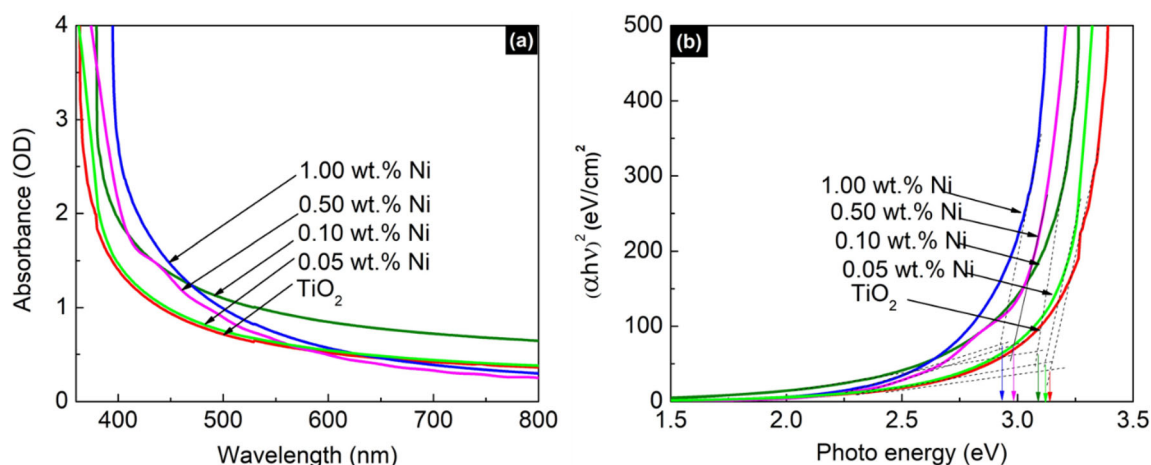


Fig. 6 UV–Visible absorption spectra of **a** un-doped, 0.05, 0.10, 0.50 and 1.00 wt% of Ni-doped TiO₂ coated films **b** dye coated un-doped, 0.05, 0.10, 0.50 and 1.00 wt% of Ni-doped TiO₂ films

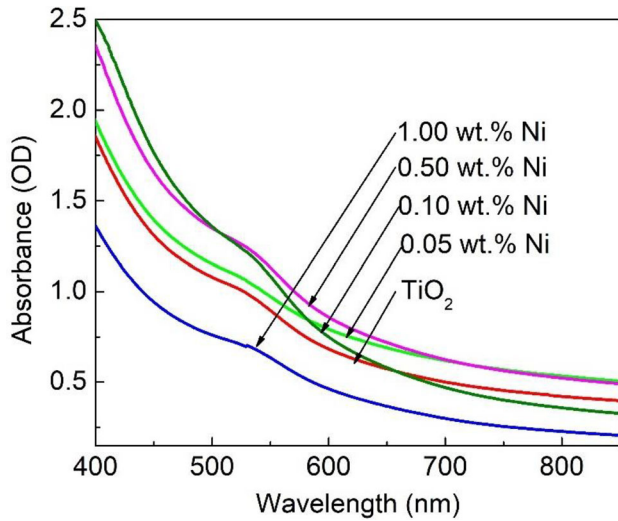


Fig. 7 UV–Visible absorption spectra of dye coated un-doped, 0.05, 0.10, 0.50 and 1.00 wt% of Ni-doped TiO₂ films

studies revealed that the PCE, especially the J_{SC} value, of TiO₂ based DSSCs is strongly affected by the amount of Ni doping (Fig. 8b). When the wt% of Ni dopant was increased, initially the J_{SC} value showed an increment from 11.90 to 12.40 mA/cm² for 0.05 wt% Ni dopant compared to the control device and then, it further increased and attained an optimum value of 13.62 mA/cm² for 0.10 wt% Ni; subsequently, the J_{SC} value showed a descending trend with further increase in Ni wt% (Fig. 8b).

The variation in J_{SC} values could be attributed to the modified surface properties of Ni-doped TiO₂ as explained earlier. In this study, the DSSC fabricated with 0.10 wt% Ni-doped TiO₂ electrode exhibited the best η of 6.29% which was around 20% improvement

Table 3 Photovoltaic parameters of the DSSCs assembled with un-doped and 0.05, 0.10, 0.50 and 1.00 wt% Ni-doped TiO₂ photoanodes under air mass (AM) 1.5 conditions (100 mWcm⁻², 1 sun)

Photoanode	J_{SC} (mA/cm ²)	V_{OC} (V)	FF	PCE (%)
Un-doped TiO ₂	11.90	0.65	0.65	5.02
0.05 wt% Ni	12.40	0.66	0.66	5.40
0.10 wt% Ni	13.62	0.67	0.69	6.29
0.50 wt% Ni	12.70	0.68	0.65	5.61
1.00 wt% Ni	11.00	0.65	0.64	4.58

compared to the control device (un-doped TiO₂ based DSSC, η = 5.02%) under air mass (AM) 1.5 conditions (100 mWcm⁻², 1 sun). In addition to the light harvesting ability, charge transport resistance also plays a major role in the device performance.

3.4 Electrochemical impedance spectroscopic (EIS) analysis

The electrochemical impedance spectroscopy was carried out to analyze the interfacial charge transfer properties of 0.10 and 1.00 wt% Ni-doped and un-doped TiO₂ based devices. The electron transport properties at each interfacial were evaluated using Nyquist plots of EIS measurements. All measurements were taken in a two-electrode system using open circuit voltage (V_{OC}) of the DSSC as the biased voltage at the frequency range between 10⁻² and 10⁶ Hz under the illumination of 100 mWcm⁻².

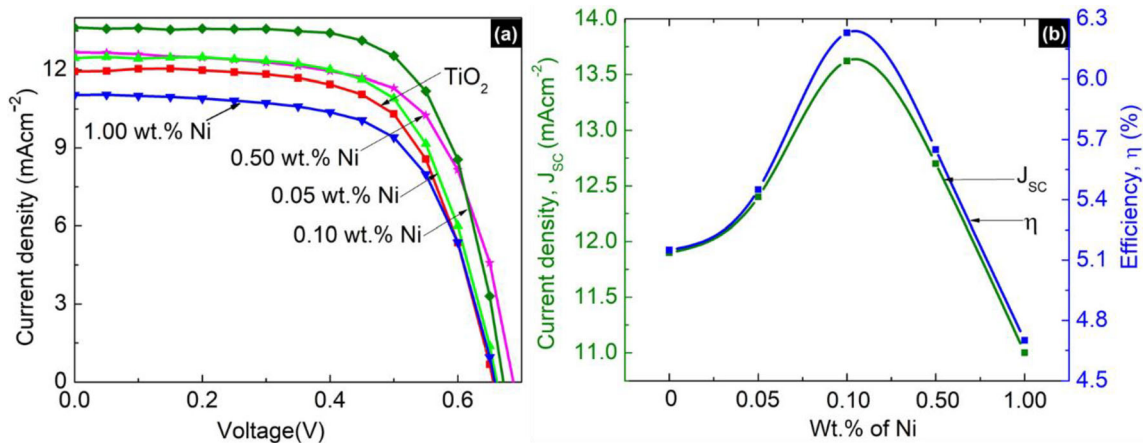


Fig. 8 **a** Current–Voltage (J–V) characteristic of the DSSCs assembled with un-doped and 0.05, 0.10, 0.50 and 1.00 wt% Ni-doped TiO₂ photoanodes, and **b** variations in J_{SC} and η with different wt% of Ni dopants under air mass (AM) 1.5 conditions (100 mWcm⁻², 1 sun)

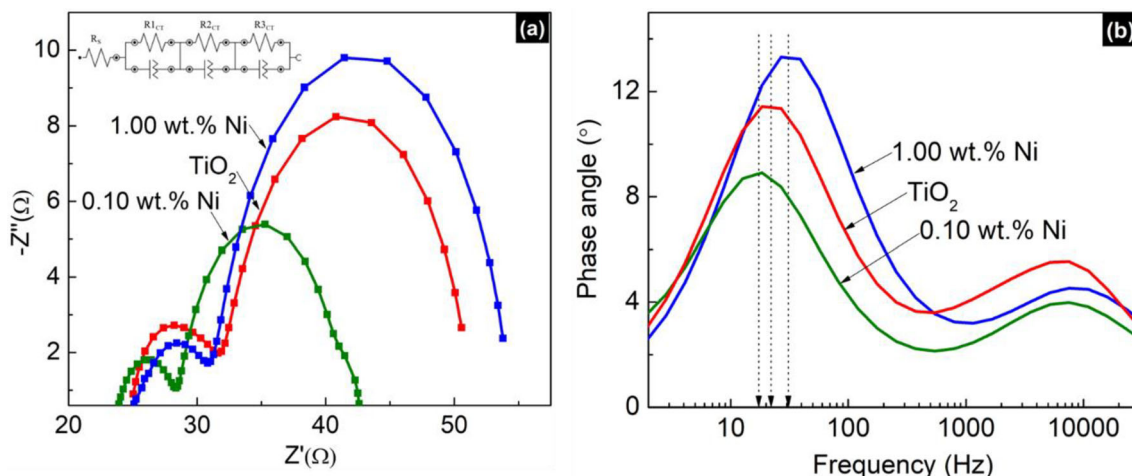


Fig. 9 **a** Nyquist plots of the DSSCs with un-doped TiO₂, 0.10 wt% and 1.00 wt% Ni-doped TiO₂ photoanodes **b** Bode plots of DSSCs based on the same photoanodes under the illumination of 100 mWcm⁻²

Table 4 Electrochemical parameters of un-doped and Ni-doped TiO₂ based DSSCs under the illumination of 100 mWcm⁻²

Photoanode	R _s (Ω)	R1 _{ct} (Ω)	R2 _{ct} (Ω)	f _{max} /Hz	T _e /ms
Un-doped TiO ₂	24.8	06.6	19.0	22.4	07.1
0.10 wt% Ni	23.9	04.4	13.0	17.0	09.3
1.00 wt% Ni	25.1	05.5	22.2	30.9	05.1

As illustrated in the Fig. 8a, series resistance (R_s) was obtained from the lower intersection point between the small semicircle and the horizontal axis of the Nyquist plot which contributed to the sheet resistance of FTO. The semicircle appears in the high-frequency region is responsible for the charge transfer resistance at the counter electrode/electrolyte interface (R1_{ct}) [38]. No significant changes were observed in the R_s and R1_{ct} values due to Ni doping. However, the charge transfer resistance of the TiO₂/dye/electrolyte interface (R2_{ct}) of the 0.10 wt% Ni-doped TiO₂ based DSSC was found to be 13.0 Ω which was lower than that of the un-doped TiO₂ based device (19.0 Ω) and led to improved charge transport at the TiO₂/dye/electrolyte interface. This is another reason for the increased J_{SC} values and enhancement in the PCEs of the Ni-doped TiO₂ based devices. Moreover, 1.00 wt% Ni-doped TiO₂ based device exhibited an increased R2_{ct} value of 22.2 Ω which indicates that higher Ni doping causes random transit flow of electrons due to the formation of intermediate trap sites. As a result of this random transition motion of electrons, charge recombination increases [19, 20]. The Bode phase plots derived from

EIS measurements on DSSCs are shown in Fig. 9b for the un-doped TiO₂, 0.10 and 1.00 wt% Ni-doped TiO₂ photoanodes. The electron life time (T_e) was estimated using the following equation:

$$T_e = \frac{1}{2\pi f_{max}}$$

where f_{max} is the maximum frequency corresponding to the peak [39, 40]. The measured electron lifetimes of the DSSCs with un-doped TiO₂, 0.10 and 1.00 wt% Ni-doped TiO₂ were found to be 7.1, 9.3 and 5.1 ms respectively (Table 4). It was noted that the electron lifetime of the DSSC with 0.1 wt% Ni-doped TiO₂ was higher than the device with un-doped TiO₂. The prolonged electron life times of the optimized 0.1 wt% Ni-doped TiO₂ based device indicates suppression of the recombination rate. This is in consistent with the previously reported study by Balakrishnan and his group [21]. It should be noted that higher Ni-doping (1.00 wt%) reduces the electron lifetime due to formation of intermediate trap sites which leads to increased charge recombination.

4 Conclusion

In this study, Ni-doped TiO₂ nanomaterials, with systematically varied Ni content from 0.05 to 1.00 wt%, were successfully synthesized by a facile impregnation method and the synthesized nanomaterials were characterized. Upon successful doping of Ni on TiO₂, anatase and rutile phases of TiO₂ were found to be retained; wavelength of light absorption showed a red shift due to reduced band gap; and dye adsorption enhanced due to increased surface area. Among the fabricated DSSCs, the device with 0.10 wt% Ni-doped TiO₂ electrode showed optimum efficiency of 6.29% with over 20% enhancement compared to the control device under air mass (AM) 1.5 conditions (100 mWcm⁻², 1 sun). This improvement in the PCE is due to the increased short circuit current density as a result of enhanced visible light harvest and improved charge transport in the device.

Acknowledgements

The authors express gratitude to the Capacity Building and Establishment of Research Consortium (CBERC) project, Grant Number LKA-3182-HRNCET and the Higher education and Research collaboration on Nanomaterials for Clean Energy Technologies (HRNCET) project, Grant number NORPART/2016/10,237 for financial support.

Author contributions

TR: Conceptualization, Methodology, Data curation, Software, Investigation, Validation, Writing—Original draft preparation, Writing—Reviewing and Editing. DV: Data curation, Investigation, Validation, Supervision, Funding acquisition, Writing—Reviewing and Editing. PR: Data curation, Investigation, Validation, Supervision, Funding acquisition, Writing—Reviewing and Editing. MS: Data curation, Investigation, Validation, Supervision, Visualization, Writing—Reviewing and Editing.

Funding

Open access funding provided by Western Norway University Of Applied Sciences. This research was funded by the Capacity Building and Establishment

of a Research Consortium (CBERC) Project (grant number LKA-3182- HRNCET) and Higher Education and Research collaboration on Nanomaterials for Clean Energy Technologies (HRNCET) Project (grant number NORPART/2016/10237).

Data availability

All data generated or analysed during this study are included in this published article.

Declarations

Conflict of interest The authors declare no conflict of interest.

Open Access This article is licensed under a Creative Commons Attribution 4.0 International License, which permits use, sharing, adaptation, distribution and reproduction in any medium or format, as long as you give appropriate credit to the original author(s) and the source, provide a link to the Creative Commons licence, and indicate if changes were made. The images or other third party material in this article are included in the article's Creative Commons licence, unless indicated otherwise in a credit line to the material. If material is not included in the article's Creative Commons licence and your intended use is not permitted by statutory regulation or exceeds the permitted use, you will need to obtain permission directly from the copyright holder. To view a copy of this licence, visit <http://creativecommons.org/licenses/by/4.0/>.

References

1. S. Borbón, S. Lugo, D. Pourjafari, N. Pineda Aguilar, G. Oskam, I. López, ACS omega **5**, 10977 (2020)
2. S. James, R. Contractor, Sci. Rep. **8**, 1 (2018)
3. S.M. Gupta, M. Tripathi, Cent. Eur. J. Chem. **10**, 279 (2012)
4. K. Prashanthan, T. Thivakarasarma, P. Ravirajan, M. Planells, N. Robertson, J. Nelson, J. Mater. Chem. C **5**, 11758 (2017)
5. T. Rajaramanan, S. Shanmugaratnam, V. Gurunathanan, S. Yohi, D. Velauthapillai, P. Ravirajan, M. Senthilnathanan, Catalysts **11**, 690 (2021)
6. A. Pirashanthan, T. Murugathas, K. Mariappan, P. Ravirajan, D. Velauthapillai, S. Yohi, Mater. Lett. **274**, 127997 (2020)

7. S. Loheeswaran, M. Thanihaichelvan, P. Ravirajan, J. Nelson, *J. Mater. Sci. : Mater. Electron.* **28**, 4732 (2017)
8. S. Loheeswaran, K. Balashangar, J. Jevirshan, P. Ravirajan, *J. Nanoelectron Optoelectron.* **8**, 484 (2013)
9. M.E. Yeoh, K.Y. Chan, *Int. J. Energy Res.* **41**, 2446 (2017)
10. Y. Zhang, L. Wang, B. Liu, J. Zhai, H. Fan, D. Wang, Y. Lin, T. Xie, *Electrochim. Acta* **56**, 6517 (2011)
11. A.K. Gupta, P. Srivastava, L. Bahadur, *Appl. Phys. A* **122**, 1 (2016)
12. X. Lü, X. Mou, J. Wu, D. Zhang, L. Zhang, F. Huang, F. Xu, S. Huang, *Adv. Funct. Mater.* **20**, 509 (2010)
13. X. Zhang, F. Liu, Q.-L. Huang, G. Zhou, Z.-S. Wang, *J. Phys. Chem. C* **115**, 12665 (2011)
14. K. Sahu, M. Dhonde, V.V.S. Murty, *Int. J. Energy Res.* **45**, 5423 (2021)
15. Y. Wang, R. Zhang, J. Li, L. Li, S. Lin, *Nanoscale Res. Lett.* **9**, 1 (2014)
16. B. Roose, S. Pathak, U. Steiner, *Chem. Soc. Rev.* **44**, 8326 (2015)
17. L.-L. Lai, W. Wen, J.-M. Wu, *RSC Adv.* **6**, 25511 (2016)
18. Y.-M. Lin, Z.-Y. Jiang, C.-Y. Zhu, X.-Y. Hu, X.-D. Zhang, J. Fan, *Mater. Chem. Phys.* **133**, 746 (2012)
19. T. Sakthivel, K.A. Kumar, J. Senthilselvan, K. Jagannathan, *J. Mater. Sci. : Mater. Electron.* **29**, 2228 (2018)
20. T. Raguram, K. Rajni, *J. Mater. Sci. : Mater. Electron.* **32**, 18264 (2021)
21. M. Balakrishnan, R. John, *J. Mater. Sci. : Mater. Electron.* **32**, 5295 (2021)
22. A. Malik, S. Hameed, M. Siddiqui, M. Haque, K. Umar, A. Khan, M. Muneer, *J. Mater. Eng. Perform.* **23**, 3184 (2014)
23. T. Rajaramanan, M. Natarajan, P. Ravirajan, M. Senthilnathanan, D. Velauthapillai, *Energies* **13**, 1532 (2020)
24. T. Karthik, R. Rathinamoorthy, R. Murugan, *J. Ind. Text.* **42**, 99 (2012)
25. S.R. Miditana, T.S. Rao, S.A. Alim, *J. Nanosci. Technol.* **5**, 682 (2019)
26. Z. Zhou, M. Li, L. Guo, *J. Phys. Chem. Solids* **71**, 1707 (2010)
27. M. Alijani, N.N. Ilkhechi, *Silicon* **10**, 2569 (2018)
28. T. Rajaramanan, F. Heidari Gourji, D. Velauthapillai, P. Ravirajan, M. Senthilnathanan, *Int. J. Energy Res.* **202**, 1090174 (2023)
29. Z. Li, D. Ding, Q. Liu, C. Ning, X. Wang, *Nanoscale Res. Lett.* **9**, 118 (2014)
30. S. Varnagiris, M. Urbonavičius, S. Sakalauskaitė, E. Demikyte, S. Tuckute, *Catalysts* **11**, 1454 (2021)
31. Z. Yao, F. Jia, S. Tian, C. Li, Z. Jiang, X. Bai, *ACS Appl. Mater. Interfaces* **2**, 2617 (2010)
32. I. Ganesh, A. Gupta, P. Kumar, P. Sekhar, K. Radha, G. Padmanabham, G. Sundararajan, *Sci. World J.* **2012**, 127326 (2012)
33. J. Manju, S.M.J. Jawhar, *J. Mater. Res.* **33**, 1534 (2018)
34. S. Prathapani, V. More, S. Bohm, P. Bhargava, A. Yella, S. Mallick, *Appl. Mater. Today* **7**, 112 (2017)
35. P. Archana, E.N. Kumar, C. Vijila, S. Ramakrishna, M. Yusoff, R. Jose, *Dalton Trans.* **42**, 1024 (2013)
36. M.R. Elahifard, S. Ahmadvand, A. Mirzanejad, *Mater. Sci. Semicond. Process.* **84**, 10 (2018)
37. P. Soni, V. Murty, K. Kushwaha, *J. Nanosci. Nanoeng Appl.* **8**, 69 (2018)
38. H.F. Mehnane et al, *RSC Adv.* **7**, 2358 (2017)
39. A. Ramar, R. Saraswathi, M. Rajkumar, S.-M. Chen, *J. Phys. Chem. C* **119**, 23830 (2015)
40. T. Nikolay, L. Larina, O. Shevaleevskiy, B.T. Ahn, in *2011 37th IEEE Photovoltaic Specialists Conference (IEEE, 2011)*, pp. 000748

Publisher's Note Springer Nature remains neutral with regard to jurisdictional claims in published maps and institutional affiliations.